Theoretical Studies and Simulation of Gold–Silica–Gold Multilayer "Fanoshells" for Sensing Applications

Luke C. Ugwuoke and Tjaart P. J. Krüger*,†

Department of Physics, University of Pretoria,

Private bag X20, Hatfield 0028, South Africa

E-mail: tjaart.kruger@up.ac.za

Phone: +27 12 420 4778. Fax: +27 12 362 5288

Abstract

We develop a theoretical framework, based on a multipole, quasi-static approach, for the prediction of the localized surface plasmon resonances in Fanoshells formed *via* geometrical symmetry-breaking in multilayer nanoshells consisting of a metallic core, a dielectric inner shell, and a metallic outer shell. By tuning the core and shell offsets of a gold–silica–gold multilayer nanoshell, we show that the theoretical model is in good agreement with electrodynamic simulations. The dipolar resonances are more suppressed when the core and the outer shell are both offset, and less suppressed when either the core, the inner shell, or the outer shell is offset. Our theoretical model allows us to relate these effects to the coupling constants arising from single symmetry-breaking. Using three performance parameters, we propose the outer shell offset as the optimal Fanoshell for sensing applications. This study systematically investigates offset-based, single symmetry-broken, metal–dielectric–metal multilayer nanoshells within the Rayleigh regime.

1 Introduction

The term *Fanoshells* was first used in Ref.[1] to refer to core-shell nanostructures capable of supporting localized surface plasmon resonances (LSPRs) with Fano-like lineshapes — LSPRs with a distortion in their spectral lineshapes that results in an LSPR shift.[1–3] These resonances, known as *Fano resonances*, are formed as a result of interference between radiant, broad-band, dipolar modes and optically dark, narrow-band, multipolar modes such as quadrupole modes.[2,4–6] However, the term "Fano resonances" has also been used to describe the plasmon resonances formed *via* the plasmon hybridization of dipolar solid sphere and nanoshell plasmons in multilayer nanoshells (MNSs).[1,7] Here, we will adopt both definitions, the latter being more relevant when there is no geometrical symmetry-breaking,[1,3,7] while the former is more relevant to symmetry-broken conventional nanoshells (CNSs)[2,8] and MNSs.[1,6,9] In these geometries, the Fano effect has been shown to occur *via* dipole-quadrupole and higher-order couplings, which cause the multipolar mode to become dipole-active, i.e., the LSPR of the dark, multipolar mode becomes enhanced and visible in the spectra, while the LSPR of the bright, dipolar mode becomes less radiant or suppressed.[1,2,6] Mode enhancement and suppression can be revealed by calculating the dipole polarizability of the Fanoshell[2,10] or the complex amplitude of the radiant, dipolar mode[1,2] in order to show that such dipole-active modes are only present in the absorption and scattering spectra of symmetry-broken CNSs[2,8,11] and MNSs.[1,9]

Fanoshells in the sub-100 nm, Rayleigh regime are experimentally realistic using wet chemistry techniques such as those reported in Refs.[4,12] Furthermore, the extinction spectra of CNSs excited with specially-designed laser beams also support Fano resonances.[3] Fanoshells have been designed *via* geometrical symmetry-breaking in both CNSs[8,13] and MNSs,[5,9] and through the use of bimetallic nanoshells.[14] Geometrical symmetry-breaking involves the introduction of some asymmetry in the arrangement of the core-shell geometry through core-offsetting,[1,2,8,9,15] shell-offsetting,[5,6] and other means, such as shell-cutting.[16] This allows solid plasmons to hybridize with cavity plasmons of both the same and different

angular momentum numbers — a phenomenon that is symmetry-forbidden in concentric nanoshells.[4,8,12] Such an approach has led to the formation of nanoeggs from CNSs,[2,4,8,11,13] a nanosphere-in-a-nanoegg from an MNS (i.e., an MNS with a metallic shell-offset[5,6]), as well as other Fanoshell configurations such as an MNS with a metallic core-offset,[1,9] and an MNS with a dielectric shell-offset.[6]

In a CNS, solid sphere plasmons of the shell hybridize with cavity sphere plasmons of the core to form bonding and anti-bonding modes.[17] The dipole moment of the anti-bonding mode is weak,[17–19] so that the subradiant, dipole-active modes in the Fanoshell of a CNS are mostly due to a Fano effect between the bonding dipole and multipolar modes.[2,4,8,11] In contrast, in an MNS, nanoshell plasmons hybridize with solid sphere plasmons of the core to form either two hybridized modes — the bonding and anti-bonding modes, such as in Au-silica-Au and Ag-silica-Au MNSs[5,12,14,20–23] — or three hybridized modes — the bonding, anti-bonding and non-bonding modes, such as in Au-silica-Ag and Ag-silica-Ag MNSs.[22–24] The dipole moment of the non-bonding mode is weak, so that it hardly undergoes any spectral shift.[22–25] However, the other two modes can be significantly enhanced, suppressed, or shifted by proper choice of geometry size and material composition. This enables MNSs to support more than one bright mode.[25–28] In a Fanoshell of an MNS, multiple LSPRs due to a Fano effect between the bonding (or anti-bonding) dipole and multipolar modes are therefore possible.[6,9]

The optical cross-sections of Fano-based nanostructures feature LSPRs with linewidths usually narrower than those in the optical cross-sections of the parent nanostructures. Their narrow linewidths are very useful for refractive index sensing since they increase the figure-of-merit of plasmonic sensors.[18,19,29–33] In addition, Fano resonances are highly sensitive to changes in the refractive index of the surrounding medium,[18,25,30] undergoing LSPR shifts that are usually in accordance with the resonance shifts in the dipolar modes of the parent nanostructure. Since Fano resonances support multiple subradiant modes, certain nanostructures have been recommended for bioimaging *via* label-free nanolithography and surface-

enhanced spectroscopy techniques.[34]

In Fanoshells of a CNS (i.e., nanoeggs[2,8,10,13]), an increase in the core offset causes an enhancement of the multipolar LSPRs and a suppression of the dipolar LSPR. Likewise, in Fanoshells of an MNS, multipolar LSPRs can also be enhanced *via* core-offsetting but the MNS geometry creates room for additional asymmetries such as inner and outer shell offsets, which are also effective for enhancing multipolar LSPRs.[5,6] Previous studies have considered Fanoshells based on a Au-silica-Au MNS with either an offset Au core[1,9,16] or an offset Au shell,[5] a Ag-silica-Ag MNS with an offset Ag core,[15] or a Ag-silica-Au MNS with an offset Ag core, an offset silica shell, or an offset Au shell.[6] The core and shell offsets break the symmetry of the MNS geometry once along a particular axis *via* either a core offset or a shell offset. For this reason, we refer to this kind of geometrical symmetry-breaking as *single symmetry-breaking*. Although geometrical symmetry-breaking involving both an offset and a shell-cutting has been referred to as *dual symmetry-breaking*,[16] only a single symmetry axis is involved and we suggest to rather use the term *concurrent-offsets symmetry breaking*. Apart from Ref.,[1] which proposed a coupled harmonic oscillator model to predict the LSPRs in a Fanoshell with a Au core offset, only simulations have as yet been used to predict the steady-state extinction spectra of the single symmetry-broken Fanoshells.

Here, we employ both simulation and theoretical approaches to predict the spectra and the coupling constants responsible for single symmetry-breaking. In addition, we introduce a Fanoshell that breaks the symmetry of the MNS geometry along the same axis *via* both core and outer shell offsets, and obtain analytically the coupling constants responsible for such single-axis symmetry-breaking involving concurrent offsets, and the formation of its LSPRs. For the first time, a systematic study is presented using a generalized matrix equation applicable to metal-dielectric-metal multilayer Fanoshells of different material composition, and geometry sizes within the Rayleigh regime. Finally, we used three performance parameters — geometrical sensitivity, spectral sensitivity, and scattering-to-absorption ratio — to predict that the outer shell offset is the optimal Fanoshell for sensing applications.

2 Theory

In this work, we employ a theoretical approach based on the quasi-static approximation of Maxwell's equations[32,35,36] and the solid-harmonic addition theorem (SHAT),[2,37] as well as electrodynamic simulations based on three-dimensional COMSOL Multiphysics® software,[38] to investigate the mode enhancement and suppression phenomena in the extinction spectra of the Fanoshells. In Refs.,[9,15] where offset cores were studied, it was shown that both x- and z-polarized incident fields lead to the same number of LSPRs in the spectra of the Fanoshell but that the latter results in slightly larger spectral shifts. Here, we will investigate the optical response of the Fanoshells to both z- and x-polarizations of the incident field but will present the spectra obtained from the former only since its LSPRs are slightly more sensitive to the offsets than the latter. The spectra obtained for $x-$polarization can be found in Fig. S3 of the Supplementary Information.

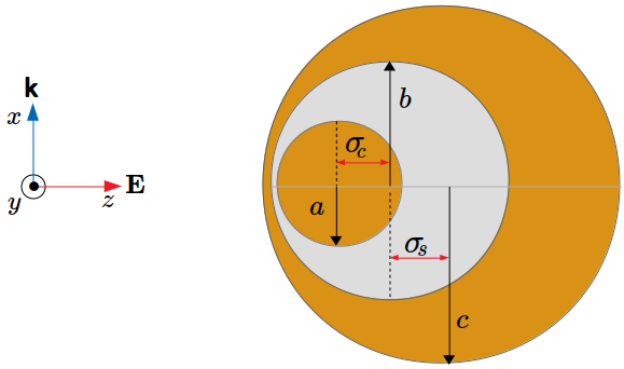

Figure 1: Model geometry of the metal-dielectric-metal MNS with a metallic core of radius a, an inner shell of radius b, giving a dielectric layer of thickness $b-a$, and an outer shell of radius c, giving a metallic layer of thickness $c-b$. An incident electric field, $\mathbf{E}$, propagating along the x-direction with a wavevector $\mathbf{k}$ is plane-polarized in the z-direction along the direction of the core and outer shell offsets, σ_c and σ_s, respectively.

We employed the approach previously used in Ref.[2] where the electrostatic potentials from the solution of the Laplace equation for a sphere in a homogeneous electrostatic field are written for each region in the Fanoshell, and the respective boundary conditions inside and outside each of these regions are matched accordingly, with the application of the SHAT[37] at the interface where any two regions share separate centers as a result of an offset. This

allows us to obtain the complex amplitude of the scattered dipole potential, F_1, in the medium surrounding the Fanoshell, from which the dynamic polarizability can be obtained from the expressions[13,39]

$$\alpha(\omega) = \alpha_s(\omega)\left[1 - \frac{k_h^2}{4\pi\varepsilon_0 c}\alpha_s(\omega) - \frac{ik_h^3}{6\pi\varepsilon_0}\alpha_s(\omega)\right]^{-1}, \tag{1a}$$

$$\alpha_s(\omega) = 4\pi\varepsilon_0 c^2 F_1/E_0, \tag{1b}$$

and the extinction efficiency of each Fanoshell *via* energy conservation:[35,40–42]

$$Q_{ext} = \frac{1}{A}\left[\frac{k_h \Im[\alpha(\omega)]}{\varepsilon_0} + \frac{k_h^4|\alpha(\omega)|^2}{6\pi\varepsilon_0^2}\right], \tag{2}$$

where $\alpha_s(\omega)$ is the quasi-static dipole polarizability, ε_0 is the free-space permittivity, A is the cross-sectional area of the MNS, and $k_h = 2\pi\sqrt{\varepsilon_h}/\lambda$ is the wavenumber of an incident field of amplitude E_0 and wavelength λ propagating in a host medium of dielectric constant ε_h.

The frequency-dependent, complex dielectric function of the metal is modelled using a Drude-Lorentz model of the form[43]

$$\varepsilon(\omega) = \varepsilon_\infty - f_0\frac{\omega_p^2}{\omega(\omega - i\gamma_p)} + \sum_{j=1}^{5} f_j \frac{\omega_p^2}{\omega_j^2 - \omega^2 + i\omega\gamma_j}, \tag{3}$$

where $\varepsilon_c(\omega) = \varepsilon_s(\omega) = \varepsilon(\omega)$ in the case of Fig. 1, $\varepsilon_c(\omega)$ and $\varepsilon_s(\omega)$ are the dielectric constants of the metallic core and shell, respectively, ε_∞ is the high-frequency dielectric constant of the positive ion core, f_0, ω_p, and γ_p are the oscillator strength, plasma frequency, and damping rate of the free electrons, respectively, j is the number of Lorentz oscillators with oscillator strength f_j, frequency ω_j, and damping rate γ_j associated with bound electrons, and ω is the frequency of the incident field. The values of these parameters for different metals can be found in Ref.[43]

To find F_1, a matrix equation with F_l unknowns is solved for l multipoles, giving (see the

Supplementary Information):

$$\sum_{n=1}^{N} p_l L_{ln} \sum_{l=1}^{N} S_{nl} v_l F_l + \sum_{n=1}^{N} q_l K_{ln} \sum_{l=1}^{N} T_{nl} v_l F_l = \sum_{n=1}^{N} p_l L_{ln} \sum_{l=1}^{N} U_{nl} + \sum_{n=1}^{N} q_l K_{ln} \sum_{l=1}^{N} V_{nl}, \quad (4)$$

where

$$S_{nl} = \tilde{c}_n M_{nl} x_l + \tilde{d}_n N_{nl}, T_{nl} = \tilde{a}_n M_{nl} x_l + \tilde{b}_n N_{nl}, \quad (5a)$$

$$U_{nl} = \tilde{c}_n M_{nl} g_l + \tilde{d}_n N_{nl} u_l, V_{nl} = \tilde{a}_n M_{nl} g_l + \tilde{b}_n N_{nl} u_l, \quad (5b)$$

$$K_{ln} = \begin{pmatrix} n \\ l \end{pmatrix} \frac{a^l \sigma_c^{n-l}}{b^n} \begin{cases} 1, & n \geq l \\ 0, & n < l \end{cases}, \quad L_{ln} = (-1)^{l-n} \begin{pmatrix} l \\ n \end{pmatrix} \frac{b^{n+1} \sigma_c^{l-n}}{a^{l+1}} \begin{cases} 1, & l \geq n \\ 0, & l < n \end{cases}, \quad (6a)$$

$$M_{nl} = \begin{pmatrix} l \\ n \end{pmatrix} \frac{b^n \sigma_s^{l-n}}{c^l} \begin{cases} 1, & l \geq n \\ 0, & l < n \end{cases}, \quad N_{nl} = (-1)^{n-l} \begin{pmatrix} n \\ l \end{pmatrix} \frac{c^{l+1} \sigma_s^{n-l}}{b^{n+1}} \begin{cases} 1, & n \geq l \\ 0, & n < l \end{cases}, \quad (6b)$$

and

$$p_l = l\varepsilon_c(\omega) + (l+1)\varepsilon_d, q_l = l[\varepsilon_c(\omega) - \varepsilon_d], \quad (7a)$$

$$\tilde{a}_n = [n\varepsilon_s(\omega) + (n+1)\varepsilon_d]/(2n+1)\varepsilon_d, \tilde{b}_n = (n+1)[\varepsilon_d - \varepsilon_s(\omega)]/(2n+1)\varepsilon_d, \quad (7b)$$

$$\tilde{c}_n = n[\varepsilon_d - \varepsilon_s(\omega)]/(2n+1)\varepsilon_d, \tilde{d}_n = [(n+1)\varepsilon_s(\omega) + n\varepsilon_d]/(2n+1)\varepsilon_d, \quad (7c)$$

$$v_l = [l\varepsilon_s(\omega) + (l+1)\varepsilon_h]/(2l+1)\varepsilon_s(\omega), g_l = y_l + u_l x_l, \quad (7d)$$

$$x_l = (l+1)[l\varepsilon_s(\omega) - \varepsilon_h]/[l\varepsilon_s(\omega) + (l+1)\varepsilon_h], \quad (7e)$$

$$y_l = E_0 c(l+2)\delta_{1l}\varepsilon_h/[l\varepsilon_s(\omega) + (l+1)\varepsilon_h], u_l = E_0 c\delta_{1l}[l\varepsilon_s(\omega) - \varepsilon_h]/(2l+1)\varepsilon_s(\omega), \quad (7f)$$

$$\delta_{1l} = \begin{cases} 1, & l = 1 \quad \text{(bright mode)} \\ 0, & l \geq 2 \quad \text{(dark modes)} \end{cases}. \quad (7g)$$

Here, K_{ln} and L_{ln} are the coupling constants between the solid plasmons of the metal core and the cavity plasmons of the dielectric shell for the same ($l = n$) and different ($l \neq n$) angular momentum numbers, respectively, M_{nl} and N_{nl} are the coupling constants between the solid plasmons of the metallic shell and the cavity plasmons of the dielectric shell for the same ($n = l$) and different ($n \neq l$) angular momentum numbers, respectively, and ε_d is the dielectric constant of the dielectric shell. The coupling constants, K_{ln} and L_{ln}, are dependent on the core radius, a, the inner shell radius, b, and the core offset, σ_c. On the other hand, the coupling constants, M_{nl} and N_{nl}, are dependent on the inner shell radius, b, the outer shell radius, c, and the shell offset, σ_s. Their dependence on the offset is shown in Fig. S2 of the Supplementary Information using the geometric parameters given in Section 3. However, their contributions in Eq. (4) are in the form of matrix elements and not as sums as indicated in Fig. S2. When there is no offset, the coupling constants K_{ln} and L_{ln} depend only on the core aspect ratio, $K_{11} = a/b$, while the coupling constants M_{ln} and N_{ln} depend only on the inner shell aspect ratio, $M_{11} = b/c$, as shown in Table 1.

The simulations were performed in the RF module of COMSOL Multiphysics using a spherically-symmetric perfectly-matched layer (PML) and scattering boundary conditions applied in the internal PML surface. A z-polarized incident plane wave, $\mathbf{E} = E_0 e^{-ik_h x}\hat{e}_z$, propagating in the x-direction was applied to the MNS. The extinction efficiency of each Fanoshell was calculated from energy conservation through the following expression:[44]

$$Q_{ext} = \frac{1}{AP_0}\left[\iiint P_{dis}dV + \iint \Re[S_{sca}]dS\right]. \tag{8}$$

The first term in Eq. (8) is a volume integral of the total power dissipation density of the nanoparticle, P_{dis}. The second term is a surface integral of the real part of the flux of the complex Poynting vector of the scattered field, S_{sca}, and P_0 is the power density of the incident field.[44]

3 Results and discussion

We studied nanoparticle sizes within the Rayleigh regime where the electrostatic approximation is valid. The following sizes were considered: $a = 25$ nm, $b = 35$ nm, $c = 45$ nm, for core and outer shell offsets in the range $0 \leq \sigma_c < b - a$ and $0 \leq \sigma_s < c - b$, respectively. We considered offsets of the core and metallic shell with respect to a fixed dielectric shell. The geometry we started with in Fig. 1 that led to Eq. (4) is of the form shown in Fig. 2**e**: a concurrent offset core and outer shell, i.e., the core offset is in the direction of the negative z-axis while the outer shell offset is in the direction of the positive z-axis, such that neither the core nor the outer shell share the same center with the inner shell. On the other hand, the offset inner shell geometry (Fig. 2**d**) requires that both the core and the outer shell are offset equally in either the direction of the positive or negative z-axis. This causes the core and the outer shell to share the same center, thereby making the inner shell offset with respect to the center of those two. The direction of the offsets in either the positive or negative z-axis does not affect the optical response of the other Fanoshell configurations.

Table 1: Offsets and coupling constants for the realization of the optical response of each Fanoshell configuration from Eq. (4).

	Fanoshell	Offsets	Coupling constants
a	No offset	$\sigma_c = \sigma_s = 0$	$K_{l=n} = \left(\frac{a}{b}\right)^n; L_{l=n} = \left(\frac{a}{b}\right)^{-(n+1)}; M_{n=l} = \left(\frac{b}{c}\right)^l; N_{n=l} = \left(\frac{b}{c}\right)^{-(l+1)}$
b	Offset core	$0 < \sigma_c < b - a, \sigma_s = 0$	$K_{ln}; L_{ln}; M_{n=l} = \left(\frac{b}{c}\right)^l; N_{n=l} = \left(\frac{b}{c}\right)^{-(l+1)}$
c	Offset outer shell	$\sigma_c = 0, 0 < \sigma_s < c - b$	$K_{l=n} = \left(\frac{a}{b}\right)^n; L_{l=n} = \left(\frac{a}{b}\right)^{-(n+1)}; M_{nl}; N_{nl}$
d	Offset inner shell	$\sigma_s = -\sigma_c, 0 < \sigma_c < b - a$	$K_{ln}; L_{ln}; M_{nl}; N_{nl}$
e	Offset core and outer shell	$0 < \sigma_c \leq \sigma_s < c - b, 0 < \sigma_s \geq \sigma_c < b - a$	$K_{ln}; L_{ln}; M_{nl}; N_{nl}$
		$0 < \sigma_c \geq \sigma_s < c - b, 0 < \sigma_s \leq \sigma_c < b - a$	$K_{ln}; L_{ln}; M_{nl}; N_{nl}$

All the combinations of no offset or a finite offset lead to the Fanoshell configurations shown in Fig. 2. Table 1 lists for each of these configurations the different values of the offsets and the coupling constants associated with their core-shell plasmons. We solved Eq. (4) for the first ten multipoles ($N = 10$), i.e., for $l, n = 1, 2, ..., 10$, using a home-developed Python-based code, with $\varepsilon_d = 2.04$ and $\varepsilon_h = 1.77$ as the dielectric constants of silica and

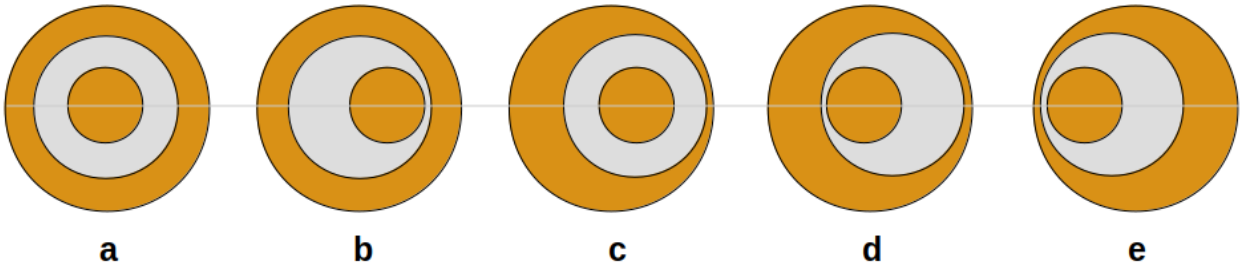

Figure 2: Fanoshells of a metal-dielectric-metal multilayer nanoshell illustrated in two dimensions. **a** No offset, **b** Offset core, **c** Offset outer shell, **d** Offset inner shell, **e** Offset core and outer shell.

water (the host medium), respectively. Thus, Eq. (4) is a generalized matrix equation, which, when combined with Eqs. (1) and (2), predicts the theoretical extinction spectra of metal–dielectric–metal multilayer Fanoshells once the dielectric constants $\varepsilon_c(\omega), \varepsilon_s(\omega), \varepsilon_d, \varepsilon_h$, the radii a, b, c, and the offsets σ_c and σ_s are given. We used Au–silica–Au Fanoshells to validate the theoretical model by comparing it with simulation results. This enabled us to draw comparisons with existing literature on Au–silica–Au Fanoshells.[1,5,9,26,28]

3.1 Mode Suppression and Enhancement

We denote the anti-bonding and bonding dipolar LSPRs by $a1$ and $b1$, respectively. Let $1, 2, 3, ...$, denote the dipole, quadrupole, octupole modes, and so on, respectively. As shown in Figs. 3 and 5 (blue curves) and in Fig. 4**a**, the Fanoshell with no offset does not support dipole-active, multipolar LSPRs. Since the coupling constants are independent of the offsets (Table 1**a**), the Fano effect fails to occur. Ref.[9] has also shown that multipolar LSPRs are dark at offsets small compared to the shell thickness. The reason for this is that the offset-dependent coupling constants in Eq. (6) are weak at small offsets. Thus, we used large offsets in this section to ensure that the multipolar peaks are visible as a result of strong coupling of the bright mode to the dark modes of the MNS. In Fig. 4**a**, the field enhancements show that although $a1$ and $b1$ are both bright (dipolar) modes, $b1$ is super-radiant while $a1$ is sub-radiant. Thus, $b1$ is more likely to contribute to the Fano effect at large offsets.

In the extinction spectra of the single-offset symmetry-broken Fanoshells shown in Fig. 3,

the theoretical model (Fig. 3(**a**-**c**)) agrees well with the simulation results (Fig. 3(**d**-**f**)). Due to the quasi-static approximation, the relative extinction efficiencies differ but the number and positions of the LSPRs predicted by both methods are very similar. In this work, we are interested in the LSPRs, especially $b1$, due to its high sensitivity to the offsets (*vide infra*). The anti-bonding dipole LSPR, $a1$, indexed around 535 nm in Fig. 3(**a**-**c**) and around 545 nm in Fig. 3(**d**-**f**), does not undergo any wavelength shift with a change in the offset.

The anti-bonding mode is formed by the hybridization of the sphere plasmons of the Au core and the anti-bonding mode of the core-shell plasmons of the silica–Au nanoshell, while the bonding mode is formed by the hybridization of the sphere plasmons of the Au core and the bonding mode of the core-shell plasmons of the silica–Au nanoshell.[9,21,28] For the size of the MNS geometry considered in this study, and other similar sizes where $b-a=c-b$, $a1$ is usually weak compared to the bonding dipole LSPR, $b1$, since the LSPR of the anti-bonding core-shell plasmons is also weak.[9,26,28] Thus, such sizes are chosen in order to preferentially enhance $b1$, since it has been shown to contribute significantly to the formation of dipole-active, multipolar LSPRs,[5,6,9] compared to geometry sizes where the enhancement of $a1$ was preferred.[5] Therefore, the inability of $a1$ to undergo mode suppression and a subsequent wavelength shift at large offsets in the single-offsets symmetry-broken Fanoshells is the result of the dipole moment of $a1$ being too weak to contribute to the offsets-dependent Fano effect.

As shown in Figs. 3 and 5, the bonding LSPRs — $b1, b2$, and $b3$ — dominate the extinction spectra of the Fanoshells, in agreement with previous literature.[5,6,9,15] Fig. 3 shows that as the offset approaches the shell thickness, $b2$ and $b3$ become more enhanced and $b1$ becomes more suppressed. This is due to an increase in the coupling constants. The Fanoshell with a Au core offset (Figs. 3**a** and 3**d**) supports a significant suppression of $b1$ and enhancement of $b2$ and $b3$ followed by the Fanoshell with a silica shell offset (Figs. 3**b** and 3**e**) and the Fanoshell with a Au shell offset (Figs. 3**c** and 3**f**). Due to this reason, the Au core offset geometry supports larger offset-dependent wavelength shifts in $b1$ compared to the other two Fanoshells. The suppression of $b1$ at large offsets in the Fanoshell with a

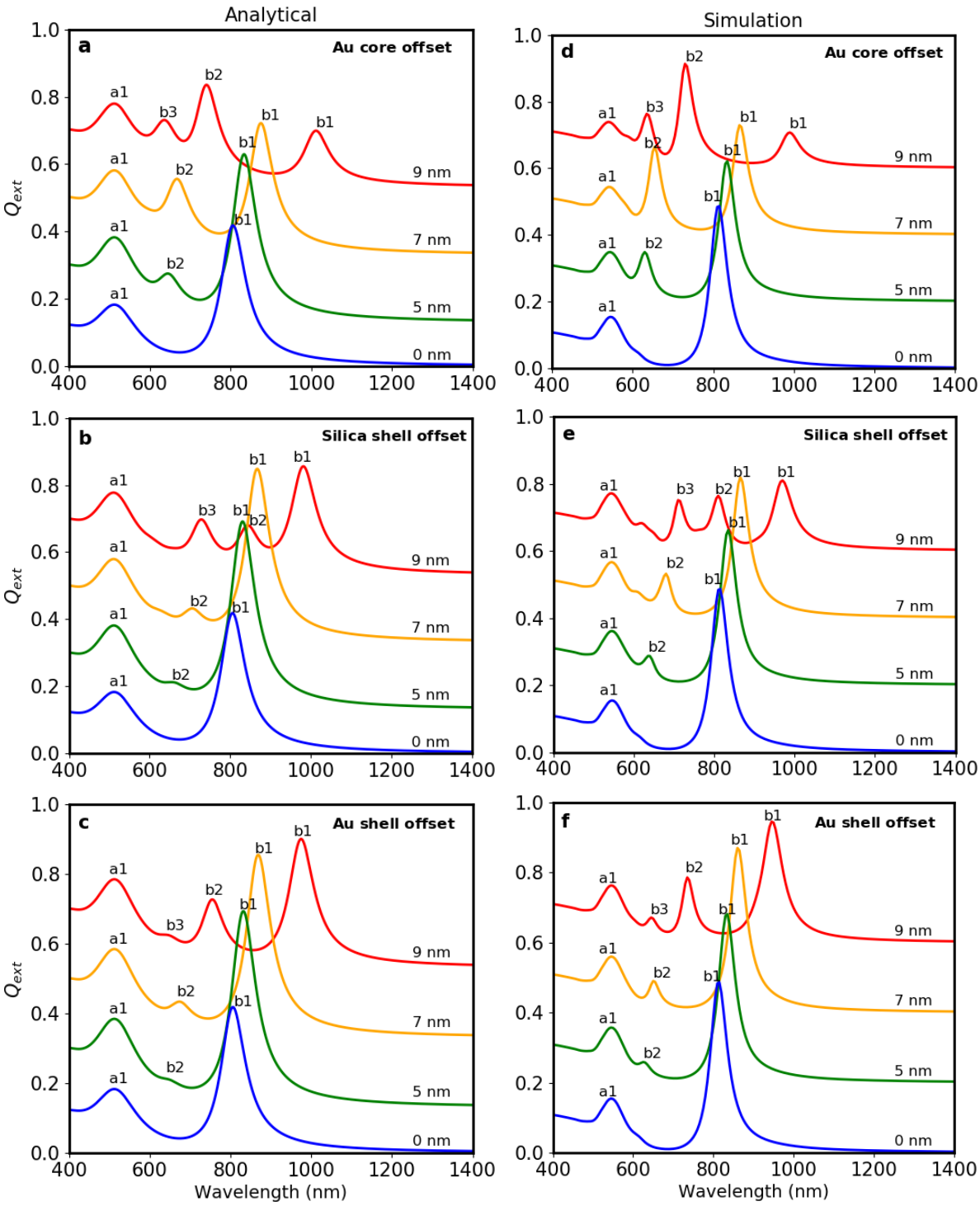

Figure 3: Normalized extinction efficiency of the single-offset symmetry-broken Fanoshells for the **a-c** analytical results and **d-f** simulation results. The spectra for 5-nm, 7-nm, and 9-nm offsets have been vertically shifted by equal amounts.

Au core offset causes $b1$ to become less radiant than $b2$ and $b3$ (Fig. 4**b**), compared to the other Fanoshells (Fig. 4**c** and Fig. 4**d**). This has been referred to as the *quenching of the radiant mode*[2]. Though both $b2$ and $b3$ become dipole-active (radiant) due to their mode-mixing with $b1$, some of their multipolar character is still present since $b1$ is not entirely quenched. This is more pronounced in Fig. 4**c** and Fig. 4**d**, where $b2$ and $b3$ are sub-radiant with respect to $b1$. However, the dark, multipolar character of $b2$ and $b3$ is only noticeable away from the core-shell overlap regions (Fig. 4), otherwise they are super-radiant near the overlap regions due to the intense localization of the scattered field.

In Figs. 3**a** and 3**d**, $b1$, indexed around 805 nm at 0-nm offset (blue curve), shifts to ∼1010 nm when the core is offset at 9-nm (red curve). This is more than the wavelength shifts in the silica shell offset where $b1$ shifts from ∼805 nm at 0-nm offset to ∼983 nm at 9-nm offset (Figs. 3**b** and 3**e**) and in the Au shell offset where it shifts from ∼805 nm at 0-nm offset to ∼976 nm at 9-nm offset (Figs. 3**c** and 3**f**).

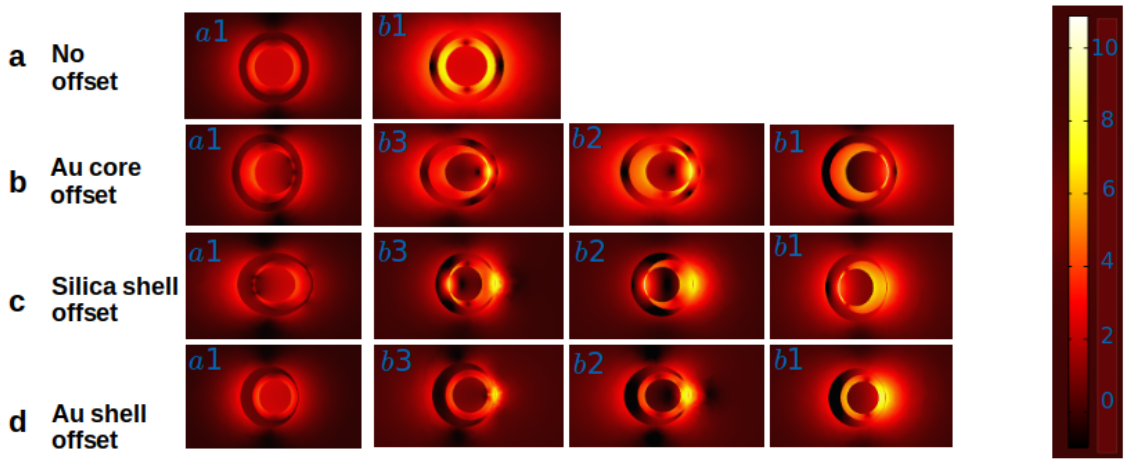

Figure 4: Colour maps of the logarithmic electric field enhancements ($log|E/E_0|^2$), at the indicated LSPR of the concentric MNS (**a**) and those of the single-offset, symmetry-broken Fanoshells (**b**, **c** and **d**), for a z-polarized incident field in the direction of the 9-nm offsets. The labels, $a1$ to $b1$, from left to right reflects the indexing in Fig. 3 (red curves).

On the other hand, the bonding multipolar LSPRs undergo larger offset-dependent wavelength shifts in Fanoshells with an offset shell. For instance, in Figs. 3**b** and 3**e** (silica shell offset), $b2$ shifts from ∼658 nm at 5-nm offset (green curve) to ∼843 nm at 9-nm offset, and

from ∼645 nm to ∼754 nm for the same offsets in the spectra of the Au shell offset (Figs. 3**c** and 3**f**). These shifts are slightly larger than the wavelength shift in the spectra of Au core offset where $b2$ shifts from ∼645 nm at 5-nm offset to ∼743 nm at 9-nm offset (Figs. 3**a** and 3**d**), because K_{ln} and L_{ln} contribute more to the enhancement of the multipolar LSPRs and wavelength shifts in the dipolar LSPR but less to the wavelength shifts in the multipolar LSPRs compared to M_{nl} and N_{nl}. In the former, all the coupling terms contribute to the extinction of the incident radiation (governed by the right hand side of Eq. (4)) while in the latter, only terms with $l = 1$ (the bright mode) contribute to the extinction, due to Eqs. (5b) and (7g). For this reason, $b2$ and $b3$ appear more radiant in the Au core-offset Fanoshell compared to $b2$ and $b3$ in the two shell-offset Fanoshells shown in Fig. 4. These Fanoshells can also support an octupole bonding LSPR, $b3$, at offsets near the shell thickness — where the terms in the coupling constants contribute the most to plasmon hybridization. This is illustrated by the 9-nm offset spectra at peak positions ∼650 nm, ∼720 nm, and ∼680 nm in Figs. 3**c** and 3**f** (Au core offset), Figs. 3**c** and 3**f** (silica shell offset), and Figs. 3**c** and 3**f** (Au shell offset), respectively.

Figs. 5**a** and 5**b** show that the Fanoshell with concurrent Au core and shell offsets supports more enhanced multipolar LSPRs as well as stronger wavelength shifts compared to the Fanoshells discussed earlier. Here, $b1$ is almost completely quenched for 9-nm offsets as shown in Fig. 6 (bottom panel), leading to a large wavelength shift from ∼805 nm at 0 nm (blue curve) to ∼1542 nm for 9-nm offsets (red curve). Similarly, $b2$ undergoes a large shift, from ∼662 nm for 5-nm offsets (green curve) to ∼914 nm for 9 nm offsets, causing it to be sub-radiant with respect to $b3$ (Fig. 6 (bottom panel)). As the offsets approach the shell thickness, higher-order LSPRs such as $b3, b4$ and $a2$ become dipole-active, as shown in Figs. 5**b** and 6. Though $b2, b3$ and $b4$ are more radiant than $b1$, their mixing with $b1$ does not entirely eliminate their multipolar character as shown by the electric field enhancements around the Fanoshell at these LSPRs compared to that of $b1$ (Fig. 6). Similarly, $a2$ is an enhanced anti-bonding quadrupole mode that is super-radiant with respect to $a1$ (Fig.

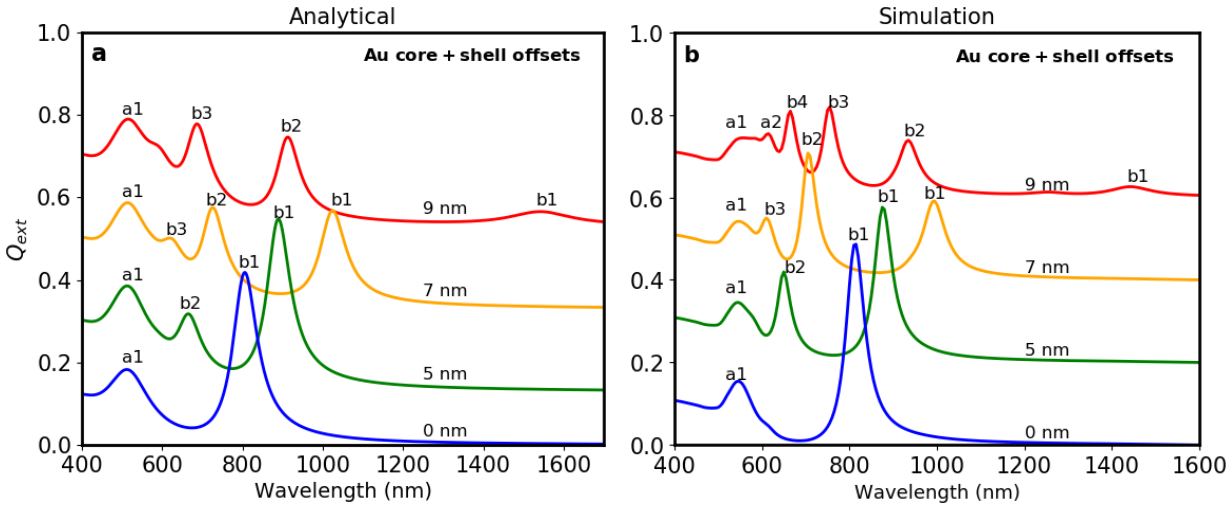

Figure 5: Normalized extinction efficiency of the concurrent-offsets symmetry-broken Fanoshell for the **a** analytical results, and **b** simulation results. The spectra for 5-nm, 7-nm, and 9-nm offsets have been vertically shifted by equal amounts.

6 (top panel)). The absence of $a2$ and $b4$ in Fig. 5**a** for 9-nm offsets shows that the simulation does not totally agree with the theoretical model for this Fanoshell at offsets comparable to the shell thickness. The LSPR, $a2$, indexed around 620 nm at 9-nm offsets, though not dipole-active in Fig. 5**a**, is visible in Fig. 5**b** due to the mode suppression of $a1$. The appearance of $a2$ and $b4$ in Fig. 5**b** at large offsets is due to the radiative damping of $a1$ and the multipolar bonding modes, $b2$ and $b3$, respectively. This pronounced radiative damping of the LSPRs at large offsets is induced when the Fanoshell's core and outer shell are concurrently offset. The modes $a2$ and $b4$ are absent in Fig. 5**a** because the polarizability in Eq. (1) is based on the Meier and Wokaun long-wavelength approximation (MWLWA) described in Ref.[39] The MWLWA does not account for the radiative damping of the multipolar modes or the short-wavelength LSPRs such as $a1$. Hence, unlike single-offset symmetry-breaking, the concurrent-offsets symmetry-breaking can cause higher-order anti-bonding LSPRs to become dipole-active, since it involves both the contribution of all the coupling constants, K_{ln}, L_{ln}, M_{nl}, and N_{nl}, to the Fano effect, and the radiative damping of $a1$. Though all the coupling constants also contribute to the formation of the multipolar LSPRs in the silica shell offset geometry, the negative shell offset (Table 1**d**) decreases the

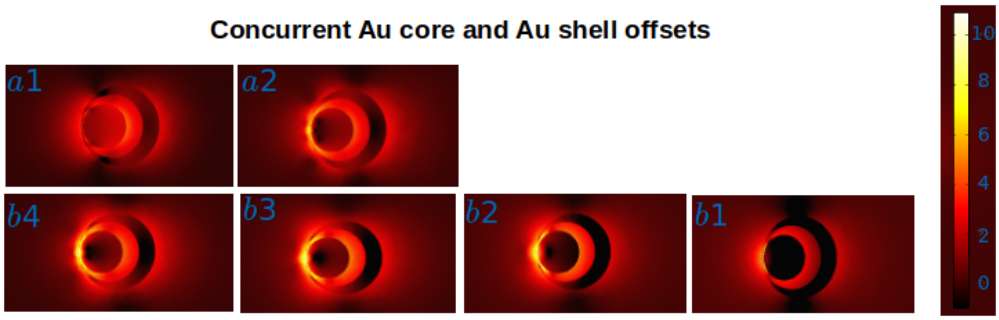

Figure 6: Colour maps of the logarithmic electric field enhancements ($log|E/E_0|^2$), at the indicated LSPR of the concurrent-offsets, symmetry-broken Fanoshell, for a z-polarized incident field in the direction of the 9-nm offsets.

coupling terms in M_{nl} and N_{nl} compared to their values with a positive shell offset (Table 1e).

3.2 Performance Parameters

In this section, we will discuss and use three performance parameters — geometrical sensitivity, spectral sensitivity, and scattering-to-absorption ratio — to determine the optimal Fanoshell for refractive index sensing. The aim of this section is not to optimize these parameters but to determine how they are affected by the Fanoshell configuration and the offset. These parameters are also affected by the size of the MNS geometry. For instance, in Ref.,[5] where an outer Au shell offset was studied, it was shown that decreasing the core size enhances the sensitivity of the multipolar LSPRs. Nevertheless, core-size dependence is not investigated here.

3.2.1 Geometrical Sensitivity

In order to determine the Fanoshell configuration most sensitive to an offset, we introduce the *geometrical sensitivity*. It measures the ease at which the LSPR responds to changes in the offset. A similar approach has been used in Ref.[28] to measure the ease at which the LSPRs respond to changes in the inner shell thickness of the no-offset Fanoshell. Fig. 7 shows the dependence of the wavelength shifts on the offset for the two most sensitive

bonding LSPRs — the dipolar (b1) and quadrupolar (b2) LSPRs. The wavelength shift in the bonding dipolar LSPR, calculated as $b1 - b1_0$, where $b1_0$ denotes the bonding dipolar LSPR of the Fanoshell with no offset, has a near-exponential growth (i.e. a redshift) with increasing offset (Fig. **7a**). This is a sharp contrast to the *universal scaling principle*,[28] according to which the wavelength shift exhibits a near-exponential decay (i.e. a blueshift) with increasing thickness of the inner dielectric shell. This inverse relationship between the universal scaling principle and offset-based, geometrical symmetry-breaking can be justified by recognizing that in the former, the coupling strength between the solid sphere plasmons of the metallic core and those of the metallic shell decreases as the thickness of the inner dielectric shell is increased, while in the latter, the coupling strengths responsible for the formation of the bonding modes, increase as the offset approaches the shell thickness, as shown in Fig. S2 of the Supplementary Information.

Let S_g denote the geometrical sensitivity or the growth rate. We can then represent the wavelength shift *via* an exponential function of the form

$$b1 - b1_0 = a_0 e^{S_g \sigma}, \tag{9}$$

where σ is the offset, and a_0 denotes the constant wavelength shift at small offsets in the range $0 < \sigma < 2$ (Fig. **7a**), where the suppression of the dipolar LSPR leads to negligible shifts. Table 2 shows that the high values of both S_g and a_0 in the Fanoshell with concurrent Au core and shell offsets are responsible for the large wavelength shifts shown in Fig. **7a** (red curve). The other Fanoshells are based on single symmetry-breaking, and can only support significant wavelength shifts at large offsets.

Fig. **7b** shows that the quadrupolar LSPRs are less sensitive to changes in the offset compared to the dipolar LSPRs. These LSPRs are not dipole-active at offsets that are small compared to the shell thickness, i.e., offsets in the range $0 < \sigma < 4$ (Fig. **7b**). At those offsets, the offset-dependent coupling constants are not sufficient to cause a Fano effect.

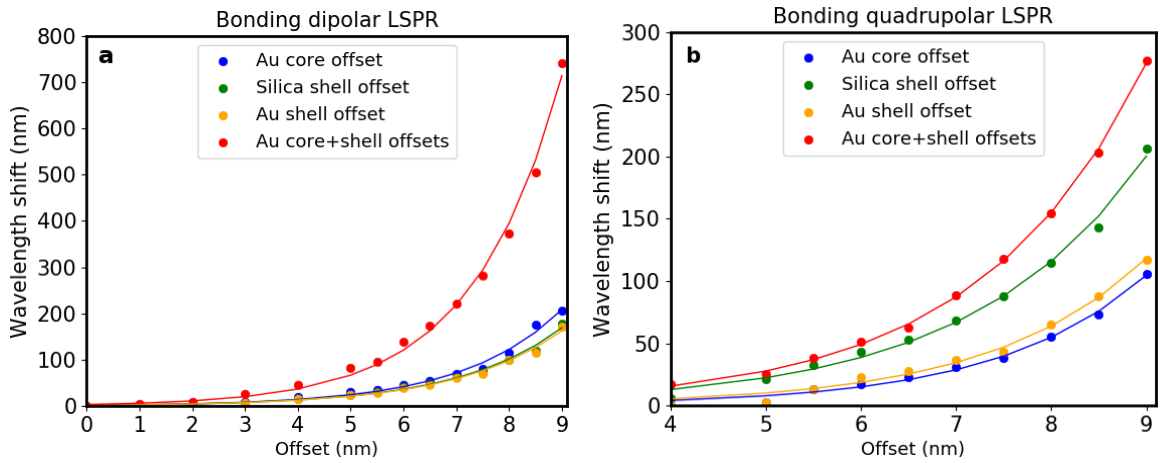

Figure 7: Dependence of the wavelength shifts of the bonding dipolar and quadrupolar LSPRs of the Fanoshells on the offset. **a** Bonding dipolar LSPR, **b** Bonding quadrupolar LSPR. Dots represent calculated LSPRs and lines are exponential fits. The wavelength shifts in **a** were calculated using the dipolar bonding LSPR of the MNS with no offset as the reference, while those in **b** were determined using the quadrupolar bonding LSPR of the MNS with a core offset at 4 nm as the reference.

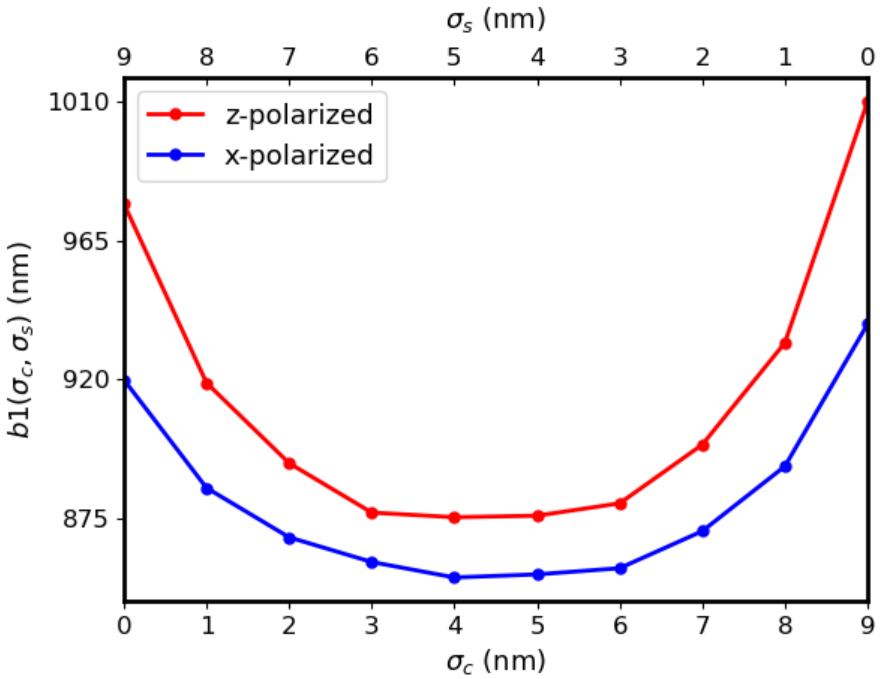

Figure 8: Dependence of the bonding dipolar LSPR, $b1(\sigma_c, \sigma_s)$, of the concurrent-offsets Fanoshell on different values of the core and shell offsets $\sigma_c \neq \sigma_s$, such that $\sigma_c + \sigma_s = 9$ nm for each (σ_c, σ_s) pair, for both the z- and x-polarizations of the incident electric field.

Fig. 7 also shows that the quadrupolar LSPRs are more sensitive to shell offsets than core offsets, while the dipolar LSPRs display the opposite behavior. This is due to the different

Table 2: Fitting parameters obtained for the Fanoshells based on the wavelength shift (Eq. (9)), for the offset-dependent bonding dipolar LSPRs (Fig. 7**a**). The standard errors in the exponential fits have been ignored.

Fanoshell	a_0 (nm)	S_g (nm^{-1})
Au core offset	1.72	0.53
Silica shell offset	1.72	0.51
Au shell offset	1.72	0.51
Au core + shell offsets	3.46	0.59

contributions from the terms in the coupling constants (see Subsection 3.1).

Fig. 8 shows the dependence of $b1$ on the polarization of the incident field when both the core and shell offsets, σ_c and σ_s, of the Fanoshell with concurrent offsets are varied. In Fig. 8, $b1$ depends specifically on a (σ_c, σ_s) pair that maximizes the offset, i.e., a (σ_c, σ_s) pair such that $\sigma_c + \sigma_s = 9$ nm. It also shows the transition of $b1$ from the maximum shell-offset only — i.e., $b1$(0 nm, 9 nm) — to the maximum core-offset only — i.e., $b1$(9 nm, 0 nm). In our theoretical model, 9 nm is the offset that leads to the largest shifts in $b1$ as we have shown in Fig. 3 and Fig. 5 (red curves). For (σ_c, σ_s) pairs where $\sigma_c + \sigma_s < 9$ nm, several permutations of σ_c and σ_s are possible, most of which do not lead to significant LSPR shifts. Beyond the 9-nm offset, the quasi-static theory performs poorly. The bonding LSPR due to the response of the Fanoshell to an x-polarized incident field is slightly blueshifted (Fig. 8, blue curve) from that of the LSPR due to a z-polarized incident field (Fig. 8, red curve). Thus, the Fanoshells are more geometrically-sensitive when the incident field is polarized in the direction of the offsets. This trend is the same for the other Fanoshells as shown in Fig. S3 of the Supplementary Information. Fig. S3 also shows that the response becomes the same when the offset is removed, showing that the polarization-dependent response is induced by the offset, in agreement with previous studies.[9] In Fig. 8, $b1$ decreases when σ_c is decreased (and σ_s is concurrently increased) until a turning point is reached in both curves where an increase in σ_s (and simultaneous decrease in σ_c) causes $b1$ to increase. However, $b1(\sigma_c > \sigma_s, \sigma_s)$ is more geometrically-sensitive than $b1(\sigma_c, \sigma_s > \sigma_c)$, in agreement with our discussions in Section 3.1. The turning point is a (σ_c, σ_s) pair that minimizes $b1(\sigma_c, \sigma_s)$

such that the matrix elements due to the pair (K_{ln}, L_{ln}) and the pair (M_{nl}, N_{nl}) contribute equally to the Fano effect at that point, else the curves in Fig. 8 will always shift toward the right (owing to a dominant contribution from the pair (K_{ln}, L_{ln})) or toward the left (due to a stronger contribution from the pair (M_{ln}, N_{ln})). For the MNS size and the offsets we considered, the turning point occurs around the pair (4 nm, 5 nm), irrespective of the incident field polarization, as shown in Fig. 8.

3.2.2 Spectral Sensitivity

The *spectral sensitivity*, S_λ,[33] also referred to as refractive index sensitivity,[25,29,30] measures the ease at which the LSPR changes with a change in the refractive index of the surrounding medium. Here, we will use $b1$, which is the most sensitive LSPR of the MNS,[25,32] to determine the most spectrally-sensitive Fanoshell. As shown in Fig. 9, $b1$ undergoes a redshift as the refractive index of the medium is increased. The values of S_λ, displayed in Table 3, are

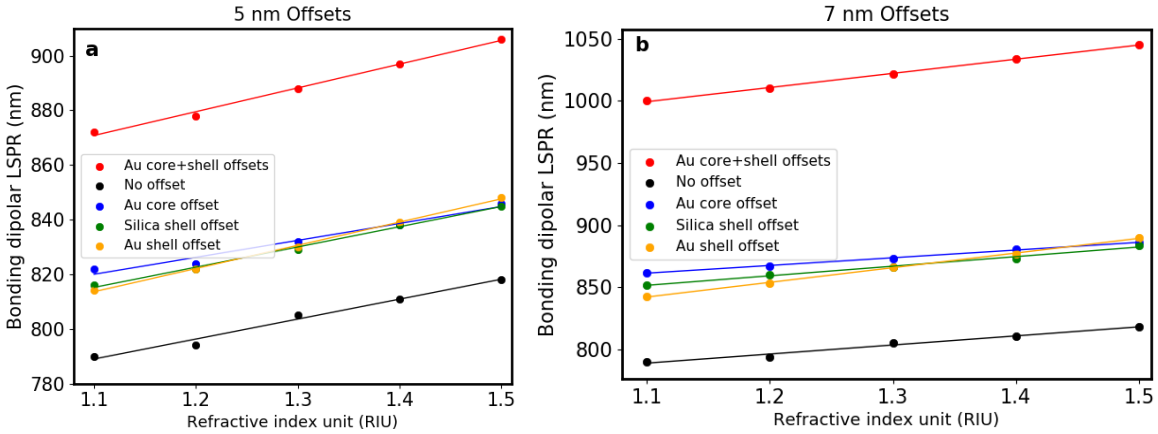

Figure 9: Dependence of the bonding dipolar LSPRs of the Fanoshells on the refractive index of the medium at **a** 5 nm offsets, and **b** 7 nm offsets. Dots represent calculated LSPRs and lines are linear fits.

obtained by fitting a linear function of the form $b1 = S_\lambda n_h + b0$,[25] to the calculated values of $b1$, where n_h is the refractive index of the host medium, and $b0$ is the vertical intercept. At 5-nm offsets, the values of S_λ are comparable for the different Fanoshells (Fig. 9**a** and Table 3 (second column)). At 7-nm offsets, the Fanoshells with Au shell offsets become

Table 3: Spectral sensitivities of the bonding dipolar LSPR obtained for the Fanoshells using linear fits. The vertical intercepts and fitting uncertainties are not included.

Fanoshell	S_λ (nmRIU^{-1}) @ 5 nm offset	S_λ (nmRIU^{-1}) @ 7 nm offset	S_λ (nmRIU^{-1}) @ 7 nm offset with a Ag core
No offset	73	73	153
Au core offset	62	63	125
Silica shell offset	74	77	150
Au shell offset	85	118	223
Au core + shell offsets	87	114	198

more spectrally-sensitive than the other Fanoshells (Fig. 9**b** and Table 3 (third column)). Curiously, the most geometrically-sensitive Fanoshell — the Fanoshell with concurrent Au core and shell offsets — is not necessarily the most spectrally-sensitive. This is likely due to two major reasons. Beside the Fanoshells being more geometrically-sensitive as the offsets approach the shell thickness, the asymmetries in Fanoshells with an outer shell offset are in direct contact with the medium while those in the core and inner shell offsets are not. Due to this reason, the Au core offset, which is the most geometrically-sensitive among the single symmetry-broken Fanoshells (Fig. 7**a**), is the least spectrally-sensitive among them, as shown in Table 3. Likewise, the Fanoshell with no offset is more spectrally-sensitive than the core-offset Fanoshell. Therefore, geometrical symmetry-breaking can be a good technique for enhancing the spectral sensitivity of MNS-based LSPR sensors only when shell offsets are involved.

3.2.3 Scattering-to-absorption ratio

The first term in Eqs. (2) and (8) is the absorption efficiency, Q_{abs}, of the nanoparticle while the second term is the scattering efficiency, Q_{sca}. Let Q_{sca}/Q_{abs} denote the scattering-to-absorption ratio. We want to determine the Fanoshell with the greatest Q_{sca}/Q_{abs} at the dipole LSPRs. Due to mode suppression, Q_{sca}/Q_{abs} of the dipolar LSPRs decreases with increasing offset (Fig. 10), in agreement with Ref.[9]

The no-offset Fanoshell (at 0-nm offset in Fig. 10) has the largest values of Q_{sca}/Q_{abs}, followed by the single symmetry-broken Fanoshells. At large offsets, where the values of

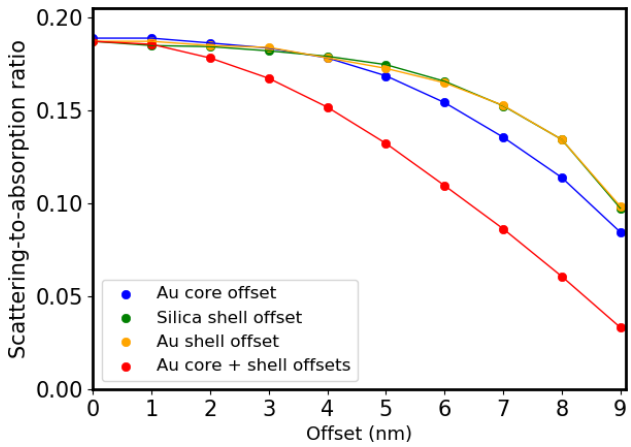

Figure 10: Dependence of the scattering-to-absorption ratio on the offset in the Fanoshells at the dipolar LSPRs. Calculated values are shown as dots connected by lines.

S_λ are high, the Fanoshells with either inner or outer shell offsets have the largest values of Q_{sca}/Q_{abs} since their dipolar LSPRs are less suppressed. Refs.[19,33] have reported that a decrease in Q_{sca}/Q_{abs} is disadvantageous for sensing applications because it has a negative impact on the resolution of the sensor. Taking also the values for S_λ in Table 3 into account, our results indicate that the outer shell offset is the optimal Fanoshell for sensing applications because at large offsets, its values for both Q_{sca}/Q_{abs} and S_λ are the highest.

The spectral sensitivities and scattering-to-absorption ratios of these Fanoshells can be further improved by using Ag-based nanostructures,[25,32] since the plasmon damping in Ag is less than that in Au.[43] The last column in Table 3 shows that there is a significant improvement in S_λ when the Au core is replaced with a Ag core. The use of other materials such as graphene[18] or other noble metals,[7,22] reduction of the core size,[5] or increasing the overall size of the MNS geometry[7,9] can enhance these parameters even further.

4 Conclusion

We have presented a generalized, multipole, quasi-static approach for the realization of multilayer Fanoshells by offsetting either the metallic core, the dielectric shell, the metallic shell, or both the metallic core and metallic shell. The equations we have derived can

be used to predict the extinction spectra of metal–dielectric–metal multilayer Fanoshells of various sizes and offsets within the quasi-static regime in significantly reduced computational time. For each offset, the analytical spectrum takes ca. half a minute to calculate via a Python code that runs on a 4 GB RAM, 1.60 GHz processor, 64-bit Intel Core i5 computer, while the simulated spectrum takes ca. 50 minutes to compute via a COMSOL model on the same computer. Using Au–silica–Au Fanoshells, we have shown analytically that the enhancement of the multipolar modes in the extinction spectra of these Fanoshells via geometrical symmetry-breaking are accompanied by the suppression of the dipolar modes, which is in good agreement with our simulations and previous studies. Our study has revealed the nature of the coupling constants responsible for mode suppression and enhancement, as well as the optimal Fanoshell for sensing applications — the outer shell offset. The study shows that in concurrent-offsets symmetry-breaking of the MNS, the coupling terms involved lead to more-enhanced multipolar LSPRs, while in single-offset symmetry-breaking, the coupling terms involved lead to less-enhanced multipolar LSPRs. For the Fanoshell sizes we studied, multipolar bonding LSPRs beyond the quadrupole LSPR become dipole-active when the offset approaches the shell thickness. Likewise, concurrent-offsets symmetry-breaking can enable the formation of visible but weak quadrupole anti-bonding LSPRs at such offsets. We attribute this to the sensitivity of the coupling constants to large offsets as well as to the radiation damping of the anti-bonding dipole mode. We also found that offset-based geometrical symmetry-breaking results in a near-exponential growth of the wavelength shifts with increasing offset, in contrast to the universal scaling principle.

Acknowledgement

The authors thank the National Research Foundation through Grant Nos. 120163 and 120387 for providing financial support for this work.

Supporting Information Available

The following files are available free of charge.

- ESI.pdf: Supplementary information containing the theoretical derivations.
- Fanoshell.py: A Python code written for the theoretical results.

References

(1) Mukherjee, S.; Sobhani, H.; Lassiter, J. B.; Bardhan, R.; Nordlander, P.; Halas, N. J. Fanoshells: Nanoparticles with Built-in Fano Resonances. *Nano Lett.* **2010**, *10*, 2694–2701.

(2) Norton, S. J.; Vo-Dinh, T. Optical Fano resonances in a nonconcentric nanoshell. *Appl. Opt.* **2016**, *10*, 2611–2618.

(3) Sancho-Parramon, J.; Jelovina, D. Boosting Fano resonances in single layer concentric core-shell particles. *Nanoscale* **2014**, *6*, 13555–13564.

(4) Wang, H.; Wu, Y.; Lassiter, B.; Nehl, C. L.; Hafner, J. H.; Nordlander, P.; Halas, N. J. Symmetry breaking in individual plasmonic nanoparticles. *Proc. Natl. Acad. Sci., USA* **2006**, *103*, 10856–10850.

(5) Qian, J.; Sun, Y.-D.; Li, Y.-D.; Xu, J.-J.; Sun, Q. Nanosphere-in-a-nanoegg: damping the high-order modes induced by symmetry breaking. *Nanoscale Res. Lett.* **2015**, *10*, doi: 10.1186/s11671–015–0728–3.

(6) Khan, A. D.; Miano, G. Fano resonance by symmetry breaking in Silver-Silica-Gold multilayer nanoshells. *In Proc. of the 8th International Conference on High-capacity Optical Networks and Emerging Technologies* **2011**, *doi: 10.1109/HONET.2011.6149823*, 233–236.

(7) Pathania, P.; Shishodia, M. S. Fano Resonance-Based Blood Plasma Monitoring and Sensing using Plasmonic Nanomatryoshka. *Plasmonics* **2021**, *16*, 2117–2124.

(8) Wu, Y.; Nordlander, P. Plasmon hybridization in nanoshells with a nonconcentric core. *J. Chem. Phys.* **2006**, *12*, 124708.

(9) Hu, Y.; Noelck, S. J.; Drezek, R. A. Symmetry Breaking in Gold-Silica-Gold Multilayer Nanoshells. *ACS Nano* **2010**, *4*, 1521–1528.

(10) Ugwuoke, L. C.; Mančal, T.; Kruger, T. P. J. Optical properties of a nanoegg-nanorod heterodimer: a quasi-static analysis. *J. Opt. Soc. Am. B* **2020**, *37*, A293 – A303.

(11) Knight, M. W.; Halas, N. J. Nanoshells to nanoeggs to nanocups: optical properties of reduced symmetry core-shell nanoparticles beyond the quasistatic limit. *New J. Phys.* **2008**, *10*, 105006.

(12) Xia, X.; Liu, Y.; Backman, V.; Ameer, G. A. Engineering sub-100 nm multi-layer nanoshells. *Nanotechnology* **2006**, *17*, 5435–5440.

(13) Zhang, J.; Zayats, A. Multiple Fano resonances in single-layer nonconcentric core-shell nanostructures. *Opt. Express* **2013**, *21*, 8426–8436.

(14) Peila-Rodriguez, O.; Pal, U. Enhanced plasmonic behavior of bimetallic (Ag-Au) multilayered spheres. *Nanoscale Res. Lett.* **2011**, *6*, 279.

(15) Ho, J. F.; Luk'yanchuk, B.; Zhang, J. B. Fano resonance in silver-silica-silver multilayer nanoshells. *Appl. Phys. A* **2012**, *107*, 133–137.

(16) Qian, J.; Chen, Z.; Wang, W.; Li, Y.; Xu, J.; Sun, Q. Dual Symmetry Breaking in Gold-Silica-Gold Multilayer Nanoshells. *Plasmonics* **2014**, *9*, 1361–1369.

(17) Prodan, E.; Nordlander, P. Plasmon hybridization in spherical nanoparticles. *J. Chem. Phys.* **2004**, *120*, 5444.

(18) Gong, S.; Xiao, B.; Xiao, L.; Tong, S.; Xiao, S.; Wang, X. Hybridization-induced dual-band tunable graphene metamaterials for sensing. *Opt. Express* **2019**, *9*, 35–43.

(19) Daneshfar, N. The Study of Scattering-to-absorption Ratio in Plasmonic Nanoparticles for Photovoltaic Cells and Sensor Applications. *Plasmonics* **2021**, *16*, 2017–2023.

(20) Bardhan, R.; Mukherjee, S.; Mirin, N. A.; Levit, S. D.; Nordlander, P.; Halas, N. J. Nanosphere-in-a-Nanoshell: A Simple Nanomatryushka. *J. Phys. Chem. C* **2010**, *114*, 7378–7383.

(21) Zhu, J.; Li, J. J.; Zhao, J. W. Tuning the dipolar plasmon hybridization of multishell metal-dielectric nanostructure: Gold nanosphere in a gold nanoshell. *Plasmonics* **2011**, *6*, 527–534.

(22) Herrera, L. J. M.; Scaffardi, L. B.; Schinca, D. C. High spectral field enhancement and tunability in core-double shell metal-dielectric-metal spherical nanoparticles. *RSC Adv.* **2016**, *6*, 110471–110481.

(23) Shirzaditabar, F.; Saliminasab, M.; Nia, B. A. Triple plasmon resonance of bimetal nanoshell. *Phys. Plasmas* **2014**, *21*, 072102.

(24) Zhu, J.; Li, J.-J.; Yuan, L.; Zhao, J.-W. Optimization of Three-Layered Au-Ag Bimetallic Nanoshells for Triple-Bands Surface Plasmon Resonance. *J. Phys. Chem. C* **2012**, *116*, 11734–11740.

(25) Katyal, J.; Soni, R. K. Localized Surface Plasmon Resonance and Refractive Index Sensitivity of Metal-Dielectric-Metal Multilayered Nanostructures. *Plasmonics* **2014**, *9*, 1171–1181.

(26) Qian, J.; Li, Y.; Chen, J.; Xu, J.; Sun, Q. Localized Hybrid Plasmon Modes Reversion in Gold-Silica-Gold Multilayer Nanoshells. *J. Phys. Chem. C* **2014**, *118*, 8581–8587.

(27) Mahmoud, M. A. Plasmon Resonance Hybridization of Gold Nanospheres and Palladium Nanoshells Combined in a Rattle Structure. *J. Phys. Chem. Lett.* **2014**, *5*, 2594–2600.

(28) Hu, Y.; Fleming, R. C.; Drezek, R. A. Optical properties of gold-silica-gold multilayer nanoshells. *Opt. Express* **2008**, *16*, 19579–19591.

(29) Lee, K.-L.; Huang, J.-B.; Chang, J.-W.; Wu, S.-H.; Wei, P.-K. Ultrasensitive Biosensors Using Enhanced Fano Resonances in Capped Gold Nanoslit Arrays. *Sci. Rep.* **2014**, *5*, 8547.

(30) Zhang, Y.; Liang, Z.; Meng, D.; Qin, Z.; Fan, Y.; Shi, X.; Smith, D. R.; Hou, E. All-dielectric refractive index sensor based on Fano resonance with high sensitivity in the mid-infrared region. *Results Phys.* **2021**, *24*, 104129.

(31) Li, X.; Shu, J.; Gu, W.; Gao, L. Deep neural network for plasmonic sensor modelling. *Opt. Mater. Express* **2019**, *9*, 3857–3862.

(32) Ma, Y.-W.; Wu, Z.-W.; Li, J.; Jiang, Y.-Y.; Yin, X.-C.; Yi, M.-F.; Zhang, L.-H. Theoretical Study on the Local Electric Field Factor and Sensitivity of Bimetallic Three-Layered Nanoshell Using Quasi-Approximation. *Plasmonics* **2021**, *16*, 2081–2090.

(33) Lee, C.; Lawrie, B.; Pooser, R.; Lee, K.-G.; Rockstuhl, C.; Tame, M. Quantum plasmonic sensors. *Chem. Rev.* **2021**, *121*, 4743–4804.

(34) Yanik, A. A.; Cetin, A. E.; Huang, M.; Artar, A.; Mousavi, S. H.; Khanikaev, A.; Connor, J. H.; Shvets, G.; Altug, H. Seeing protein monolayers with naked eye through plasmonic Fano resonances. *Proc. Natl. Acad. Sci., USA* **2011**, *108*, 11784–11789.

(35) Maier, S. A. *Plasmonics: fundamentals and applications.*; Springer science & Business media, 2007.

(36) Neeves, A. E.; Birnboim, M. H. Composite structures for the enhancement of nonlinear-optical susceptibility. *J. Opt. Soc. Am. B.* **1989**, *6*, 787–796.

(37) Caola, M. J. Solid harmonics and their addition theorems. *J. Phys. A: Math. Gen.* **1978**, *11*, L23–L26.

(38) Inc., C. COMSOL Multiphysics® v. 5.6. *http://www.comsol.com/products/multiphysics/* **2020**, *Comsol AB, Stockholm, Sweden*.

(39) Moroz, A. Depolarization field of spheroidal particles. *J. Opt. Soc. Am. B* **2009**, *26*, 517–527.

(40) Bohren, C. F.; Huffman, D. R. *Absorption and scattering of light by small particles*; John Wiley and Sons, Inc., 2008.

(41) Kreibig, U.; Genzel, L. Optical absorption of small metal particles. *Surf. Sci.* **1985**, *156*, 678–700.

(42) Barnes, W. L. Particle plasmons: Why shape matters. *Am. J. Phys.* **2016**, *84*, 593.

(43) Rakic, A. D.; Djurisic, A. B.; Elaser, J. M.; Majewski, M. L. Optical properties of metallic films for vertical-cavity optoelectronic devices. *Appl. Opt.* **1998**, *37*, 5271–5283.

(44) Grand, J.; Ru, E. L. Practical implementation of accurate finite-element calculations for electromagnetic scattering by nanoparticles. *Plasmonics* **2020**, *15*, 109–121.